Journal of Nuclear Materials 597 (2024) 155135

Contents lists available at ScienceDirect

Journal of Nuclear Materials

journal homepage: www.elsevier.com/locate/jnucmat

Influence of heat treatments on low-power-LPBFed CuCrZr for nuclear fusion applications

Valentina Candela [a,b,*], Luca Zanini [c], Marialaura Tocci [c], Massimiliano Bonesso [b], Carlo Scian [d], Mourad El Idrissi [e], Giacomo Favero [b,f], Michele Ballan [e], Stefano Corradetti [e], Razvan Dima [b], Girogio Keppel [e], Simone Mancin [f], Adriano Pepato [b], Piergiorgio Sonato [g,h]

[a] Centro Ricerche Fusione, University of Padova, Corso Stati Uniti 4, Padova 35127, Italy
[b] National Institute for Nuclear Physics (INFN) – Padua Division, via Marzolo 8, Padova 35131, Italy
[c] Department of Mechanical and Industrial Engineering, University of Brescia, via Branze 38, Brescia 25123, Italy
[d] Department of Physics and Astronomy Galileo Galilei, University of Padova, via F. Marzolo 8, Padova 35131, Italy
[e] National Institute for Nuclear Physics (INFN) - National Laboratories of Legnaro, viale dell'Università 2, Legnaro PD 35020, Italy
[f] Department of Management and Engineering, University of Padova, Str.lla S. Nicola 3, Vicenza 36100, Italy
[g] Department of Industrial Engineering, University of Padova, Via Gradenigo 6a, Padova 35131, Italy
[h] Consorzio RFX (CNR, ENEA, INFN, University of Padova, Acciaierie Venete SpA), Corso Stati Uniti, 4, Padova 35127, Italy

HIGHLIGHTS

- Additive manufacturing of CuCrZr alloy for nuclear fusion applications.
- Influence of heat treatments on CuCrZr microstructure.
- Performance evaluation of CuCrZr printed with 370 W IR laser.

ARTICLE INFO

Keywords:
LPBF
Copper alloys
Heat treatments
Microstructure
DSC
Mechanical properties

ABSTRACT

In this study, the processability of CuCrZr alloy with additive manufacturing (AM) technology and the performance achievable with Direct Age Hardening treatments for nuclear fusion applications were investigated. This copper alloy is one of the most interesting for the field: it is easier to manufacture through Laser-based additive manufacturing technology and mechanically superior compared to pure copper, and it ensures values of thermal conductivity high enough to be considered a valid substitute for pure copper in many applications.

The investigation on CuCrZr alloy was carried out in order to examine the influence of Direct Age Hardening (DAH) treatments on physical and mechanical properties. Laser Powder Bed Fusion technology was used to produce samples with CuCrZr alloy. The additive manufacturing process involved a machine provided with a 370 W IR laser and a preliminary process optimization was carried out to find the printing parameters that assured the highest density (99.15 %), which confirmed the processability of CuCrZr alloy also with low IR laser power. Then, three different DAH treatments were tested and the performance of DAHed material was compared to that of the alloy in as-built conditions. Precipitation phenomena were investigated with DSC analyses, revealing the effectiveness of the treatment already after 1 h. A deep microstructural investigation revealed a fine cellular structure formed during solidification and the presence of nanometric precipitates starting from the as-built condition. The presence of microstructural defects was also investigated. Mechanical performance and thermal conductivity were tested, too: the as-built samples showed limited properties, while very promising results for the use of additively manufactured CuCrZr components have been obtained after the DAHs. The ultimate tensile strength (UTS) and yield strength (YS) doubled the as-built values after 1 h treatment at 550 °C. The thermal conductivity reached three times the initial condition (from 100 W/mK to 300 W/mK).

* Corresponding author.
E-mail address: valentina.candela@phd.unipd.it (V. Candela).

https://doi.org/10.1016/j.jnucmat.2024.155135
Received 10 February 2024; Received in revised form 6 April 2024; Accepted 26 April 2024
Available online 27 April 2024

1. Introduction

CuCrZr (C18150) is a very attractive alloy that can substitute pure copper in many applications. The presence of Cr can range from 0.5 wt% to 1.2 wt% while the Zr can be present in the range 0.03–0.3 wt% [1]. In some cases, the alloy must satisfy compositional specifications, as it happens for nuclear fusion components foreseen in ITER (International Thermonuclear Experimental Reactor) [2–8]. CuCrZr is a precipitation-hardened alloy that is well-known for its high mechanical, thermal and electrical properties [1]. This alloy is widely used in heat exchange devices and in the nuclear fusion field for the same scope [1]. CuCrZr started being employed in reactors as a structural material for plasma-facing components in Tore Supra and JET, while in ITER it will be used to manufacture a heat sink for the divertor, for the first wall and the blanket [9–11]. The material will be employed also in DTT (Divertor Tokamak Test) facility for the same purposes as in ITER. Moreover, additive manufacturing will be tested as the manufacturing process for producing some complex designed components for DTT Neutral Beam Injector (NBI), and in particular the acceleration grids, which need to be geometrically precise and very complex. Generally, an acceleration grid consists of an actively cooled copper plate characterized by many beamlets apertures. The apertures are aimed at focusing the ions beam on a specific aiming point placed at an optimal distance, inside the vacuum vessel. The active cooling is guaranteed by internal channels with optimized shape to maximize heat exchange. In some cases, as in the Extraction Grid (EG), several grooves are also present for placing permanent magnets that create a magnetic field for deflecting the co-extracted electrons [12]. A detailed description of the design of an NBI and its ongoing development for DTT can be found in the literature [13–15]. In the preliminary conceptual design, the acceleration grids were meant to be made of pure copper, and produced by means of electrodeposition over a copper-milled base plate [15]. Copper is an FCC metal that melts at 1080 °C, it is widely used in many industrial sectors because of its excellent thermal and electrical conductivities and good corrosion resistance [16]. However, due to the poor mechanical properties of pure copper, CuCrZr alloy was chosen as an alternative material for the purpose. This study is aimed at evaluating possible heat treatments for additively manufactured parts made of CuCrZr alloy.

Additive Manufacturing (AM) is a wide family of various manufacturing techniques that share a common principle, which is exactly the opposite of traditional technologies: parts are created by adding material step after step. This allows the creation of more complex parts since the technology does not use any tools: in most cases, the hindrance of the tools or the overall manufacturing approach cannot permit the creation of very complex and peculiar shapes, which are, on the contrary, possible and easy to obtain with additive manufacturing.

With AM, the use of copper is experiencing significant advancements, as topological optimization can overcome the geometric constraints inherent in parts produced with traditional technologies. The process for pure copper is, however, very difficult, especially if the AM technology uses electromagnetic radiation as the energy input to melt the powder feedstock. In fact, in the so-called Laser Based Powder Bed Fusion process (PBF-LB/M, also known as Laser Powder Bed Fusion – LPBF or Selective Laser Melting – SLM), the material is melted thanks to the energy transferred by a laser beam. Machines are usually equipped with infrared (IR) lasers, typically operating with wavelengths ranging from 1060 to 1100 nm. This can cause several drawbacks for processing certain materials due to their high reflectivity, resulting in the dissipation of most of the energy. Copper and copper alloys are characterized by this issue [2-5,16], moreover, their thermal conductivity causes a fast cooling of the area: the printing is consequently very challenging because the resulting molten pool is easily unstable and uneven. The final microstructure is too porous and inadequate for most of the applications requiring good mechanical resistance.

Because of these difficulties, printing copper with a satisfying dense structure is possible by increasing the amount of energy that the material receives, by employing a high-power laser beam or by changing the laser wavelength, for which the material is less reflective. Nevertheless, several studies analyzed the possibility of providing coatings to the particles to enhance the optical absorption and create an *in-situ* alloying when the powder is melted (i.e. Jadhav et al. [6]). Studies can be found in the literature for both these aspects [5–7].

If pure copper is not a requirement for the application, it is possible to opt for a copper alloy, that is in most cases mechanically superior. The alloying elements are typically less reflective in the IR range compared to copper, and the manufacturing process is much easier even with a low energy input. Another advantage of the alloys is that their properties can be tailored by heat treatments [2]. Generally, the addition of elements like Cr, Zr or Nb in a copper matrix seems to greatly enhance the absorption of the laser energy, and adding two of those elements can lead to the formation of binary and ternary systems with Cu that also improve the material physical properties [2].

The advantage of CuCrZr alloy, as already mentioned, is the possibility to tailor its properties according to the specific heat treatments performed on the material. This alloy is strengthened by the precipitation of hardening particles, such as Cu_xCr_y, Cu_nZr_m, or more complex compounds like $Cu_aCr_bZr_c$ (general formulas were used because of the wide variety of intermetallic phases).

Their lattice can be more or less coherent with the Cu matrix and their presence leads to an increase in mechanical properties since they alter the lattice structure [2,3] and hinder the mobility of the dislocations. Solution Annealing (SA) and Age Hardening (AH) are the main treatments that can be performed on wrought CuCrZr, while in the case of the LPBFed material, the solution annealing can be skipped. Here are briefly described the two heat treatments for CuCrZr:

- Solution Annealing (SA): this treatment is carried out by heating the material in a protective and inert atmosphere (typically Ar) above 900 °C for 30 min or some hours. Then the material is rapidly cooled in water or air, in order to oversaturate the copper matrix with Cr and Zr [17]. In this way, the material can be subsequently aged to make the precipitation occur. In the case of LPBFed parts, this treatment is facultative since the cooling of the molten pool is fast enough to act as a quench and create an oversaturated microstructure [1]. SAed parts are very soft and mechanically too weak to consider the SA a stand-alone thermal treatment.
- Age Hardening (AH): generally, this treatment follows the SA, and it is performed at lower temperatures and for a longer time (usually from 400 to 600 °C, up to 6 h) in an inert environment (Ar, vacuum, N_2, and sometimes also in an H_2 atmosphere). This treatment is aimed at allowing controlled precipitation of hard intermetallic phases from the oversaturated material to produce binary or ternary compounds of Cu, Cr and Zr [17]. In additively manufactured pieces, as mentioned, AH can be directly performed after manufacturing, in this case, it is called Direct Age Hardening (DAH).

In this work, only DAHs were investigated. In particular, three different durations were examined keeping the temperature fixed at 550 °C. The aim is to understand how the heat treatment duration affects the material and if a DAH treatment could be suitable for reaching the mechanical and thermal conductivity requirements for the employment of additively manufactured CuCrZr for nuclear fusion reactor components. As guidelines, mechanical properties should reach an UTS of ~400 MPa, a Yield Strength YS of ~300 MPa and a rupture elongation El.% > 15%, (reference values were taken from [18]), while the thermal conductivity should be greater than 360 W/mK.

2. Materials and methods

A powder of CuCrZr alloy was used to manufacture the samples investigated in the present study. The chemical composition of the powder is reported in Table 1. The Particle Size Distribution (PSD) was

Table 1
Chemical composition of the CuCrZr powder employed in this study.

	Cu	Cr	Zr	Fe	Si	Others
Weight [wt%]	98.9	0.88	0.06	<0.03	<0.05	<0.01

D_{10} = 13.8 μm, D_{50}= 33.2 μm and D_{90} = 59.9 μm. The volume fraction and a SEM image of the virgin powder are reported in Fig. 1a and Fig. 1b, respectively.

The machine used in this work is the EOSINT M280 (Electro Optical System GmbH, Germany). It is equipped with a low power Yb:YAG laser (maximum nominal power: 400 W, actual power: 370 W, with a wavelength of 1064 nm), with a Gaussian spot diameter of approximately 100 μm.

For this study, the samples used for the material characterization were printed with a near-net shape geometry. For tensile tests and thermal conductivity measurements, samples were then machined in order to remove the rough skin and bring the samples to the correct geometrical dimensions.

2.1. Parameters optimization and density measurements

First, a parameter optimization was carried out in order to reach the highest density in the as-built samples. The best combination between hatching distance (in the range of 0.06–0.1 mm) and laser speed (from 350 to 650 mm/s) was investigated. The laser power was maintained at 370 W and the stripes width was fixed at 5 mm (a schematic view of the process is reported in Fig. 2). The layer thickness for all the jobs was 0.03 mm.

40 cubes (10 mm x 10 mm x 10 mm) were produced with different hatching-scan speed combinations. Their density was then measured by means of the Archimedes method through a ME Mettler Toledo analytical scale (Mettler Toledo GmbH, Germany).

The material reference density was measured through a gas pycnometer (AccuPyc II 1340, Micromeritics Instruments Corporation, USA).

2.2. Heat-treatments

Three direct age hardening (DAH) treatments were investigated. The treatments were performed on as-built samples in Nitrogen atmosphere, with heating and cooling ramps of 150 °C/h (cooling was carried out inside the oven, in a protected atmosphere). The DAHs were carried out at 550 °C for 1 h, 3 h and 6 h. The authors decided to stay at 550 °C as a trade-off between the development of good mechanical properties (that can be improved with DAHs at lower T) and good thermal properties (that are promoted if high temperatures are used).

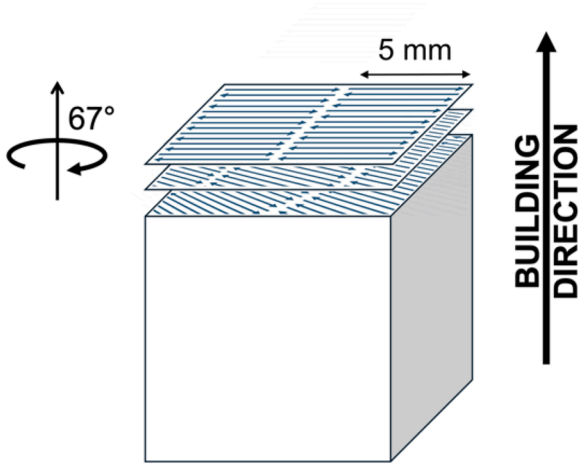

Fig. 2. Schematic view of the additive manufacturing process: stripes for this work have been set to 5 mm; at each layer, the stripes orientation varies with a rotation of 67° The vertical direction in this work coincides with the building direction.

2.3. Microstructural investigations

Vertical and horizontal cross-sections of samples in each condition were polished up to mirror finish according to standard metallographic practices. To highlight microstructural features, samples were etched with a solution containing 1.5 g of $FeCl_3$, 10 ml of HCl and 30 ml of distilled H_2O for 15–35 s. Specimens were observed under optical microscope (OM) Leica DM4 M (Leica, Germany). Samples were also observed under a Zeiss Sigma HD FEG (Carl Zeiss GmbH, Germany) and a TESCAN Vega3 (Tescan Group, Czech Republic) SEM microscopes, micrographs were taken both in back-scattered and secondary electrons modes.

2.4. DSC analysis

Calorimetric analysis was carried out on as-built and heat-treated samples in order to identify solid-state transformations in the samples, such as the formation or dissolution of precipitates. In detail, the alloy was first investigated as virgin powder and under as-built conditions, then the same analysis was carried out on samples aged at 550 °C for 1 h and 6 h as representative heat-treated conditions (minimum and maximum treatment duration). For each scan, 30 mg of material were used. Samples were heated up to 1250 °C with a heating rate of 10 °C/min under a continuous Ar flow to ensure the presence of an inert atmosphere during testing. The instrumentation used for the study was a

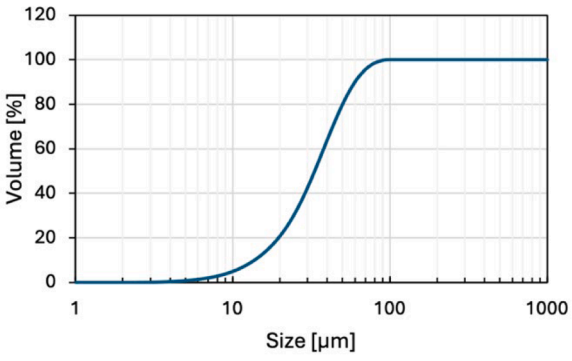

a

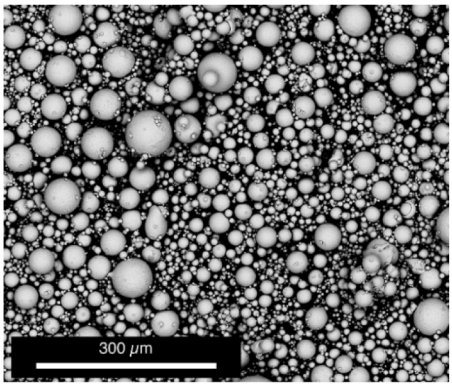

b

Fig. 1. a) Volume fraction of the CuCrZr powder investigated; b) Back-scattered SEM image of the material.

TA Instrument Q600 apparatus (TA Instrument, Delaware, USA), equipped with Universal Analysis 2000 software.

2.5. XRD investigations

Philips X'Pert PRO diffractometer (Malvern PANalytical, United Kingdom) was employed for this analysis. The unprocessed powder and the as-built samples in horizontal and vertical planes were examined. A Brag-Brentano geometry in theta-2theta XRD mode analysis was carried out in the range of 35–85° The radiation employed was Cu Kα (1.5406 Å, accelerating voltage= 40 kV, current= 40 mA). A polar scanning was also carried out.

A texture evaluation was done on the as-built (AB) samples, measuring the diffraction intensity with constant 2θ at several angular orientations. The Cu planes (111) and (220) were examined.

2.6. Micro-hardness

Vickers micro-hardness evaluation was carried out on mirror-polished samples. Random measurements were collected on both the horizontal and the vertical cross sections (directions are related to the building growth) for each investigated condition.

A 15 s dwell time with a load of 0.3 kgf was investigated. A Mitutoyo HM-200 Vickers tester (Mitutoyo, Japan) was employed for the test.

For each sample, average hardness values and relative standard deviation were calculated.

2.7. Tensile tests

The tensile tests were carried out on specimens with a final geometry defined by the ISO-6892 standard. Tensile bars were printed with a near-net shape. They were then machined to reach the correct dimensions. The tensile test machine employed was an Instron 3369 (equipped with a load cell of 50 kN). A knife edge extensometer was fixed on the gauge length of the samples to record the elongation during the test. The elongation speed was set to 1 mm/min in the elastic field and 2 mm/min in the plastic field. Three specimens were tested for each condition and vertical/horizontal direction, thus a total of 24 (12 horizontally + 12 vertically built) samples were examined. The geometry of the tensile specimens is reported in Fig. 3. For each strain-stress curve obtained, the ultimate tensile strength UTS, the yield strength YS, the elastic modulus E and the total elongation El.% were assessed. For each parameter, average values and standard deviation were calculated.

2.8. Thermal conductivity

The thermal conductivity tests were performed based on the Guarded-Comparative-Longitudinal heat flow technique [ref. ASTM E1225 – 20]. For the study, pure copper reference samples with known thermal conductivity (369 W/mK) were used. The reference values were obtained through the laser flash method [ref. ASTM E1461–13]. The samples for this test are cylindrical, with a 1 cm^2 cross-sectional area, and provided with four thermocouple holes (see Fig. 4 for construction details) to measure the temperature at different points along the sample length. The experimental setup is characterized by a hot and a cold source and the samples are placed in between to recreate a one-dimensional condition (the system was insulated from the environment using glass wool). The Fourier's law (1) can be applied and the thermal conductivity k of the unknown material measured.

$$|q| = k \cdot \frac{dT}{dx} \tag{1}$$

Where: q is the heat flux [W/m^2], k is the thermal conductivity [W/mK], T is the temperature [K], and x is the position along the cylinder axis [m].

The sample has threads for connecting it to the experimental setup and reducing the thermal resistances between the contact interfaces.

Two test pieces for the heat-treated and the as-built conditions were tested: one built in vertical and one built in horizontal direction. A total number of 8 samples were examined at three different heat fluxes, the results were then obtained by computing the average value.

3. Results

3.1. Parameter optimization and density measurements

The best manufacturing parameters were those that yielded the highest density for the cubic samples. The histogram in Fig. 5 shows the average relative density measured with the Archimedes method for all the investigated combinations of process parameters. The reference density obtained from a powder sample by the gas pycnometer was equal to 8.8869 g/cm^3. This value was used afterward to calculate the relative density of the additively manufactured samples.

The highest relative density (99.15 %) was achieved using the following set of process parameters: laser power 370 W, hatching distance 0.07 mm, scanning speed 450 mm/s, and stripes width 5 mm. The relative density did not change significantly increasing the scanning speed at 0.07 mm of hatching distance. In fact, scanning speed of 550 mm/s or 650 mm/s offered a relative density above 99 %, but 450 mm/s was chosen to investigate further the properties of the manufactured material since it ensured the highest density. Therefore, all the specimens for mechanical and thermal properties were manufactured with this combination of manufacturing parameters in order to ensure the maximum density.

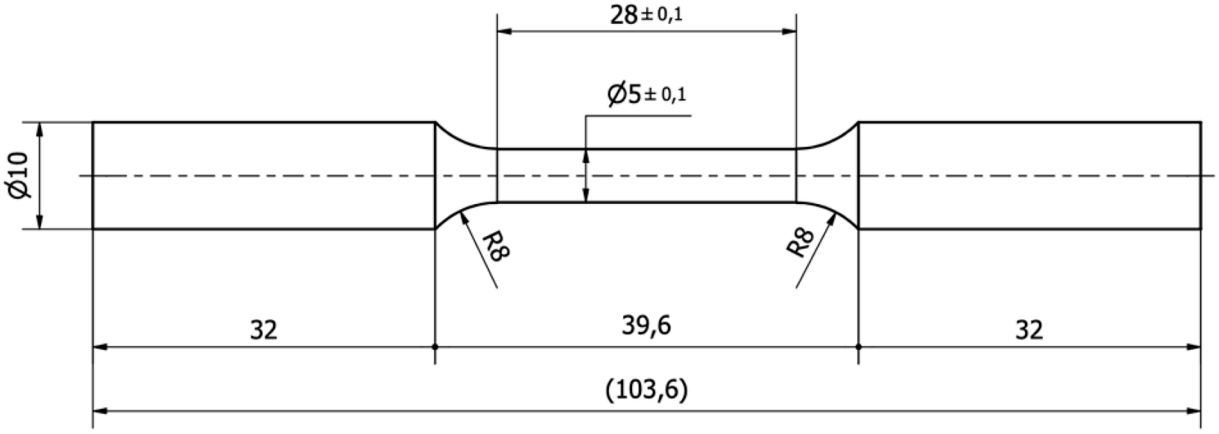

Fig. 3. Test piece dimensions [mm].

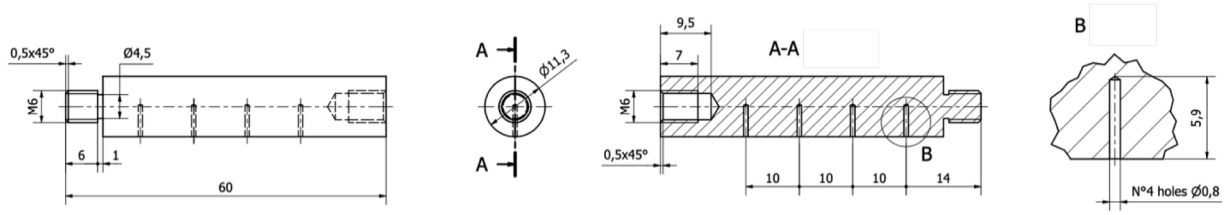

Fig. 4. Thermal conductivity test piece dimensions [mm].

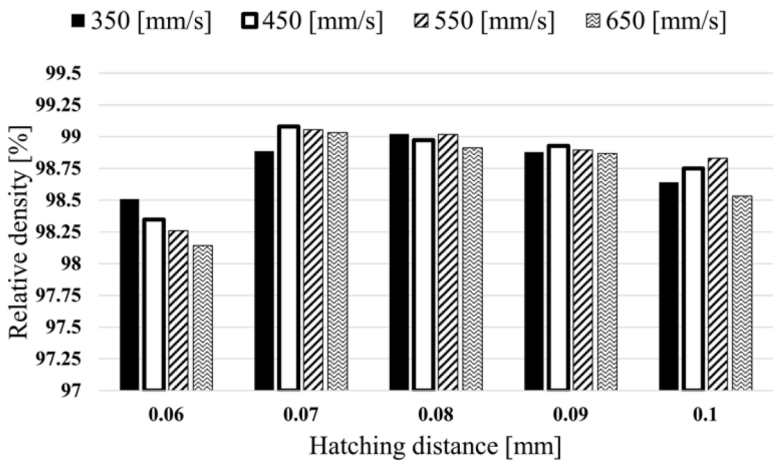

Fig. 5. Relative density of the investigated samples as a function of process parameters.

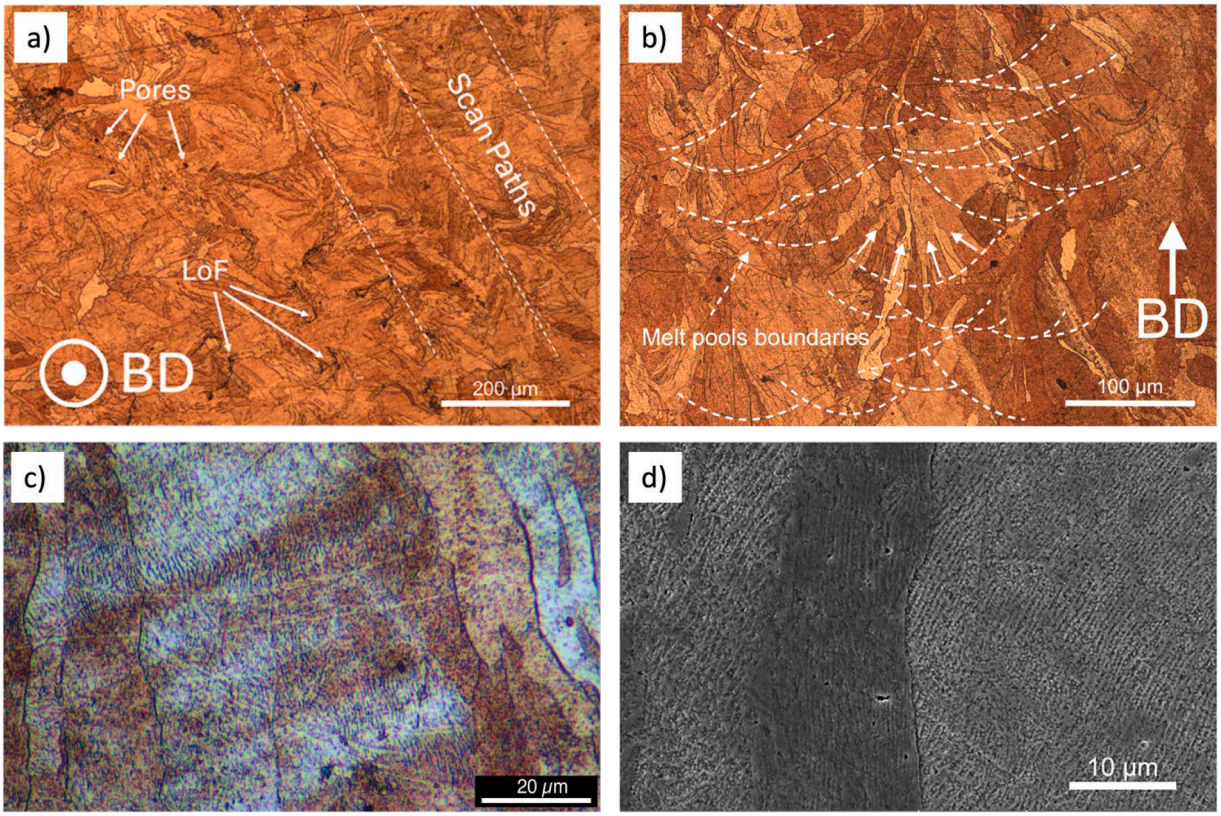

Fig. 6. Micrographs of as-built sample: a) horizontal cross-section, b) vertical cross-section c) vertical cross-section at higher magnification and d) SEM image of vertical cross-section.

A hatch distance of 0.06 mm resulted to be detrimental for the density, yielding values of density in the range 98–98.5%. This is likely due to the heat accumulation that created overheating and keyhole porosity, reducing the final density.

3.2. Microstructural investigations

Through optical and electron microscopy, it was possible to identify the presence of the scan tracks, the melt pool boundaries and the typical defects of LPBFed parts such as lack of fusion (LoF) porosities and gas pores. Both horizontal and vertical cross-sections of as-built and heat-treated parts were investigated.

In Fig. 6a, a micrograph of the horizontal cross-section of the as-built sample is reported. It is possible to clearly distinguish the scan paths, with the grains that grew following the typical morphology developed during the solidification of the molten pool, and some defects like pores (small, round and randomly dispersed across the polished surface) and LoF porosities (elongated discontinuities).

These defects can be also seen in the etched vertical cross-section of the as-built CuCrZr sample reported in Fig. 6b. Here, the melt pool boundaries were observed, as well as the grains. In particular, in the center of Fig. 6b, some grains grew perpendicularly to a melt pool boundary. These grew directed along the thermal gradient due to the high cooling rate during printing [1].

In Fig. 6c it is possible to see the overlapping of the molten pools layer after layer as thin, rounded, and brighter lines. Grains are elongated and grow along the building direction, while a fine cellular substructure is visible, whose orientation may vary between two adjacent grains. A closeup in Fig. 6d (SEM image) shows the different cellular substructure orientations that two adjacent grains developed during solidification.

This is commonly observed also in other metals printed through LPBF technique, like Ti6Al4V [19] or superalloys [20,21] that have BCC or FCC microstructure [21]. The substructure grains typology depends on the solidification rate and the magnitude of the thermal gradient [22].

The heat treatments of Direct Age Hardening did not modify the microstructural features that can be observed at low magnification, as shown in Fig. 7, where 1 h DAH and 6 h DAH samples are shown for comparison. The microstructure of both the horizontal and vertical cross-sections after DAHs did not change compared to the as-built conditions (Fig. 6): this is reasonable because, as can be seen in Fig. 8, the columnar substructure is still visible after a DAH of 6 h, indicating that the thermal energy provided during the DAH treatments, is not enough to let the re-crystallization occur.

In Fig. 8, SEM micrographs at different magnifications of the 6h-long DAH microstructure are reported. Among the columnar grains, many rounded particles are visible (especially in Fig. 8c), which could be nanometric hardening particles.

A further investigation of these nanosized precipitates was carried out: some small round particles can be seen at high magnifications, and they could be small Cr or Zr precipitates. Due to their small dimensions, EDS analyses were not possible. However, these features were seen already in as-built condition and not only after DAHs. In Fig. 9 were reported images taken on the vertical cross-section of an as-built sample, while in Fig. 10a there is the 3 h DAHed sample: a closeup on a grain boundary revealed the presence of some particles that are highlighted with dashed circles. Similarly, Fig. 10b reports what was observed in the 6 h DAHed sample.

The aspect of those round bumps is similar in all cases, regardless of the heat treatment, and they differ from the rest of the surrounding material. They could be nanosized particles made of Cr and Zr compounds.

Their size ranges from some nanometers up to more than 50 nm. In

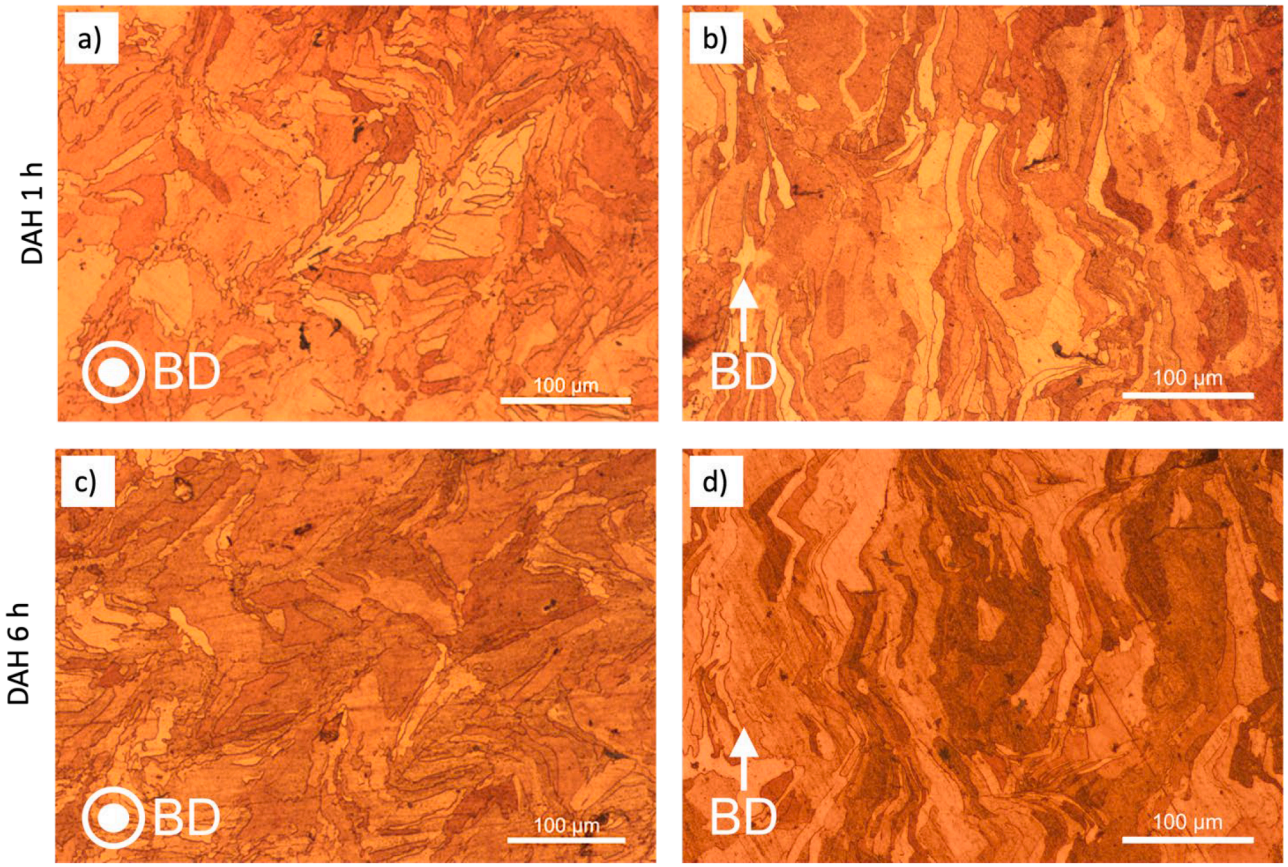

Fig. 7. Micrographs of 1 h DAH and 6 h DAH samples along vertical and horizontal cross-section.

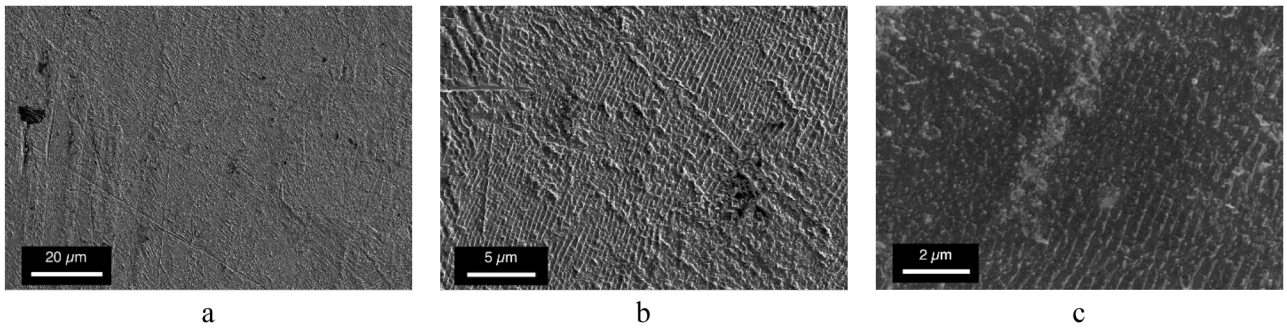

Fig. 8. SEM Secondary electron images of etched CuCrZr, heat treated at 550 °C for 6 h, at different magnifications.

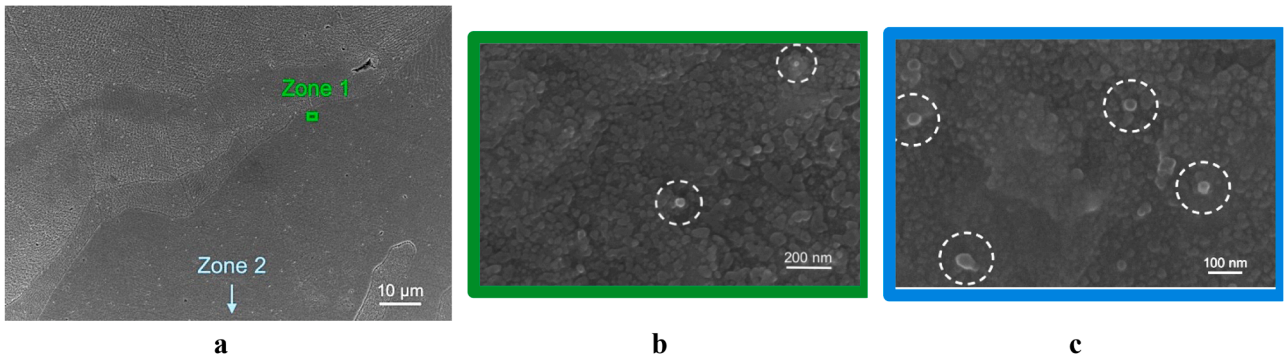

Fig. 9. a) General overview of a vertical cross-section of the as-manufactured material, b) and c) are high magnification micrographs of two zones where small round particles can be seen.

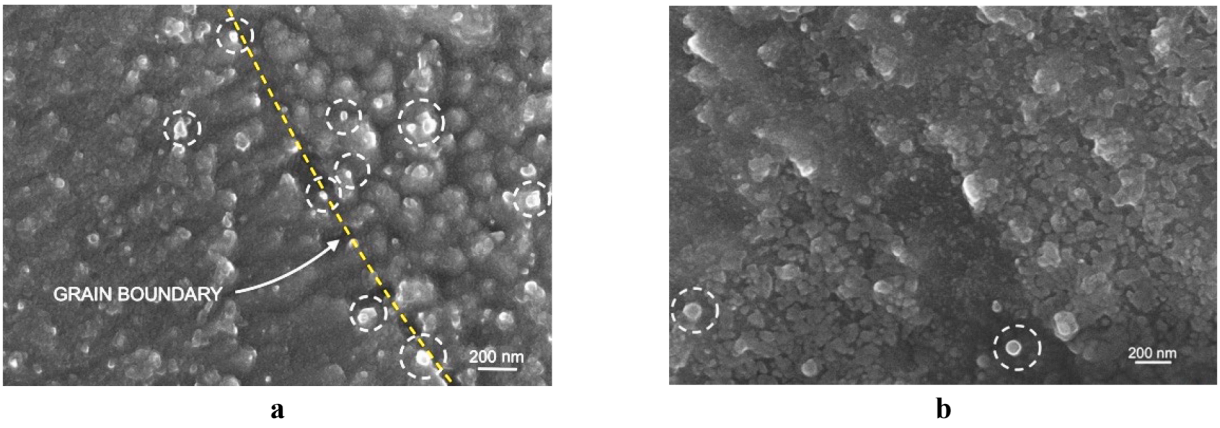

Fig. 10. a) CuCrZr heat-treated at 550 °C for 3 h, b) CuCrZr after 6 h of direct age hardening treatment.

DAHed they are slightly bigger than in the as-built parts. The particles observed are evenly dispersed inside the material, which means that there are no preferential sites where they developed in higher concentrations like the grain boundaries, as usually happens in the case of SA+AH parts. It was difficult to estimate the amount of those particles, but they appeared slightly more numerous in the 3 h DAHed sample.

As already mentioned, SEM-EDS analyses could not be carried out because of the small size of these particles, since the interaction volume involved in EDS exceeds the particle dimensions. However, detailed TEM investigations were performed by Li et al. [23] on LPBFed CuCrZr, in which they observed similar features: the dimensions and morphology are compatible with what was found in this work. Their analyses revealed the presence of Zr-rich precipitates of about 30 nm in diameter in the as-built material. Their findings are in good agreement with what has been observed in this work. In addition, the presence of precipitates in as-built conditions was confirmed also by other studies available in literature [24–26]. In particular, Xu et al. [24] have found precipitates developed with a core-shell mechanism, in which the Cr is surrounded by the Zr, however, the Zr content is much higher than the Cr. Generally, 30–100 nm are the standard dimensions of the Cr-Zr particles observed in literature.

Defects were also observed in the investigated samples. An overview of the main defects is given in this paragraph. Some defects that have been observed are typical in AMed components, such as Lack of Fusion (LoF) and porosity that is generated mainly by the gas entrapment. An example is reported in Fig. 11, the micrograph was taken from the as-built sample, in the vertical cross-section.

In addition, some regions rich in Cr and Zr were observed inside the copper matrix (Secondary and Back Scattered electrons images of a region rich in Cr from a 3 h DAHed sample are reported in Fig. 12). The

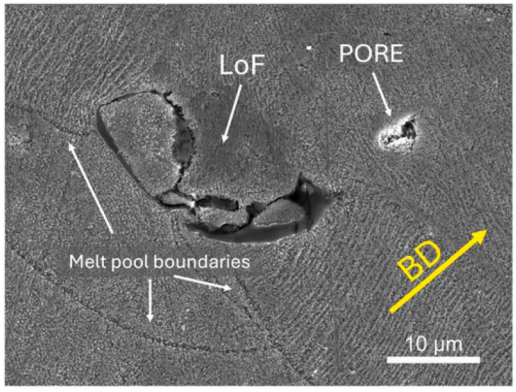

Fig. 11. Closeup on defects in the vertical cross-section of the as-built sample, melt pool boundaries are also visible.

EDS analysis shows the presence of oxygen. Presumably, O was already partly dispersed inside the material. Cr, Zr and O were always combined together. The Cu signal could derive from the surrounding material since the electron beam has an interaction volume that could have reached the copper matrix underneath.

These structures were not frequent, but they were randomly dispersed across the material in all the examined samples. In most cases, it was possible to distinguish two configurations of the Cr-Zr regions and an example can be seen in Fig. 13 (for a convention, they will be called Type I and Type II):

- Type I appears like a pseudo-continuous film that isolates a single grain from the surrounding matrix. The thickness can change and can be up to some microns.
- The Type II configuration that was observed was an inclusion that possessed very sharp and well-defined edges: such a configuration, for their geometry, is probably not produced during the rapid cooling of the molten CuCrZr.

Such structures were observed in all the samples (as-built, DAH1, DAH2 and DAH3): their presence and morphology do not depend on the thermal history of the post-printed parts, as expected since DAHs cannot change further the macroscopic morphology of the material [27] (after DAHs the material is modified at nanometric level only).

Wallis et al. [27] found randomly dispersed intermetallic phases similar to the Cr and Zr-rich regions here presented.

3.3. DSC analysis

Thermograms from DSC analysis are shown in Fig. 14.

An evident endothermic peak is visible at 1075–1085 °C for all the investigated samples (Fig. 14a). This is consistent with the melting temperature reported for the investigated alloy. This peak is particularly sharp for the alloy powder, indicating its homogeneous composition.

DSC thermograms are also useful for studying the formation of precipitates in the investigated alloy (Fig. 14b). In this regard, for the as-built sample (and for the powder sample), exothermic peaks are visible around 400 °C and in the range 500–550 °C. The first evident peak (peak temperature = 414 °C) is associated with the formation of Cr precipitates, as reported in the literature [28,29]. These precipitates play a major role in the strengthening mechanism of this alloy [27,30]. Peaks at higher temperatures are more difficult to interpret. Likely these correspond to precipitation of Cu-Zr precipitates, such as the Cu_3Zr or the $Cu_{51}Zr_{14}$ phase [31]. The stoichiometry of these phases is related to the local concentration of Zr and a precise identification is not possible based only on DSC thermograms.

Nevertheless, it is interesting to observe that these peaks are not present in the curves related to heat-treated samples, already after 1 h of heat treatment. In fact, DSC curves for samples after 1 h and 6 h aging at 550 °C are almost flat and no evident peaks can be identified. This indicates that most of the precipitation has been completed after 1 h

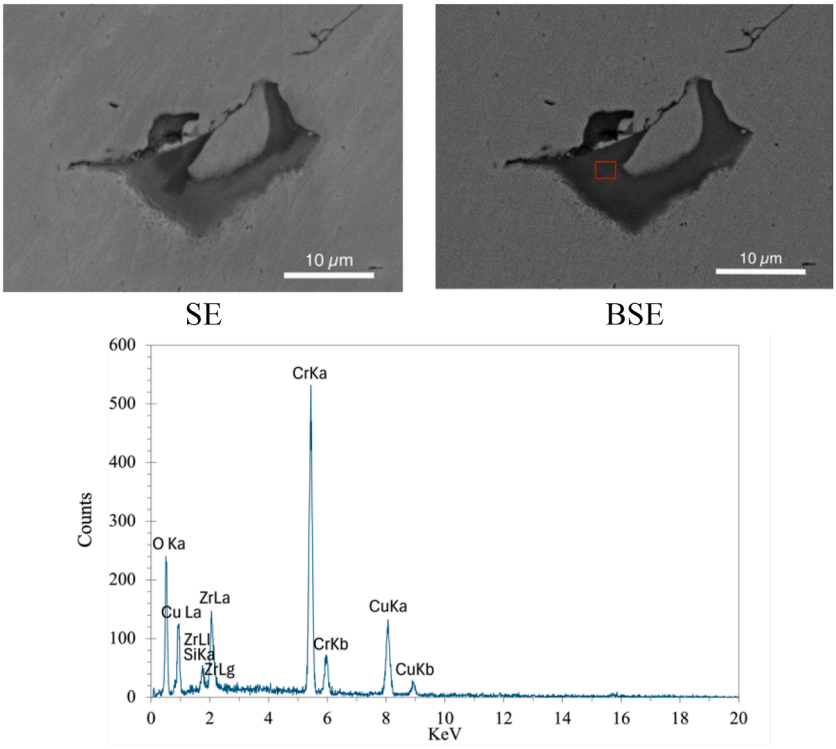

Fig. 12. Region rich in Cr inside sample treated at 550 °C for 3 h, images were taken with secondary electrons (left) and Backscattered (right), the EDS spectrum was taken on the region inside the red rectangle.

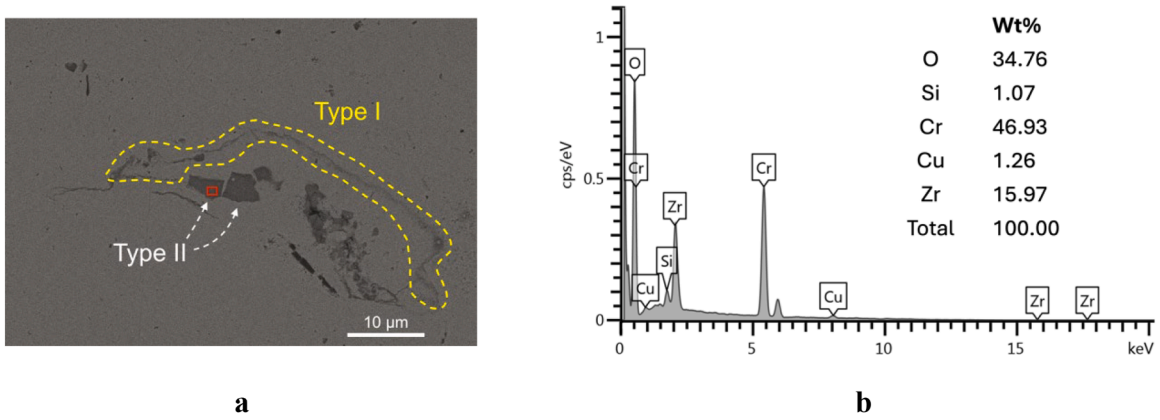

Fig. 13. a) Back-scattered electron images of the horizontal surfaces for as-built sample: Cr-Zr-O inside the copper matrix, this image was captured investigating the as-built sample, there are both Types I and II: the Cr-Zr can be seen as precipitated at the grain boundary and as bulky inclusions in the middle b) EDS analysis made on Type II particles, the investigated region is marked with the red rectangle.

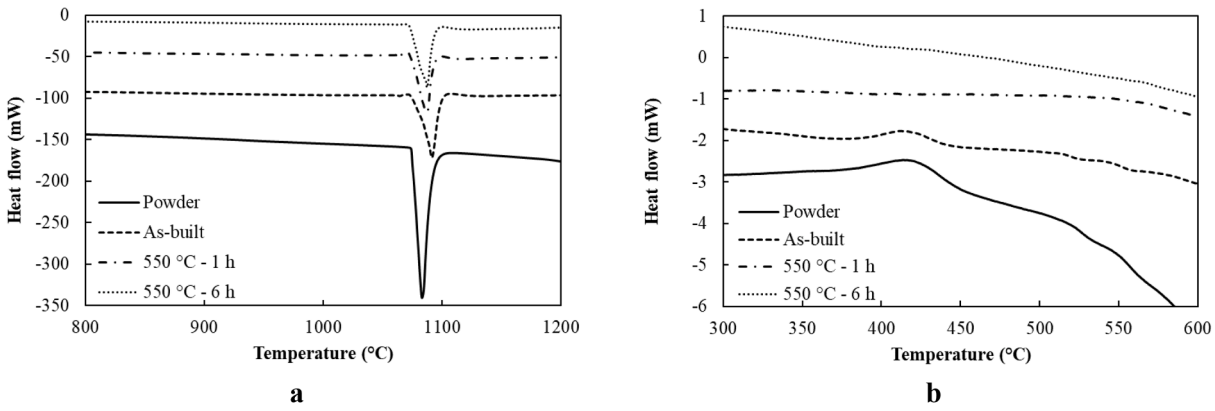

Fig. 14. DSC thermograms for the investigated alloys: a) focus on high temperature peaks, b) magnification of precipitation peaks.

treatment and no additional amount (or negligible amount) of Cr and Zr are available in solid solution to form additional strengthening particles.

3.4. XRD investigations

The as-built and DAHed samples were examined, but their diffractogram did not show differences, so the diffractogram for the as-built part is reported in Fig. 15 only and compared with the signal generated by the virgin powder.

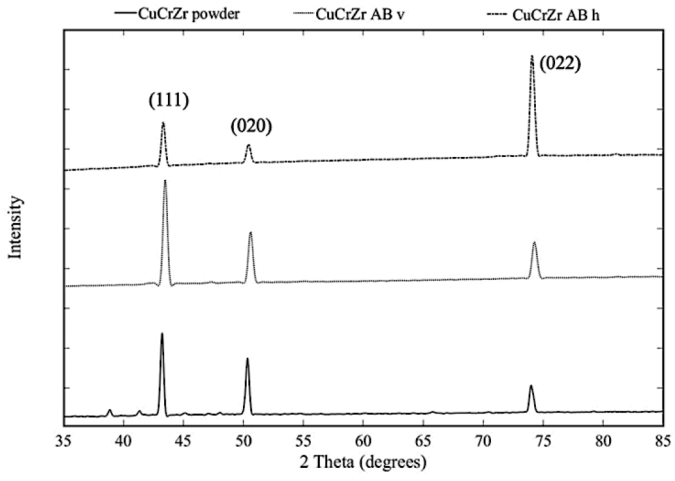

Fig. 15. XRD diffractogram for the virgin powder and the as-built samples, scanned in horizontal and vertical directions.

Cu peaks are the most evident, in particular, referred to the plane (111) at 43.2°, the plane (020) at 50.3° and the plane (022) at 74° [32]. The peaks position changed slightly depending on the examined samples, this might be due to the different morphology (powder or printed material) and the internal residual stresses. Concerning the powder, other peaks are visible at 38.9° and 41.3° (Fig. 16a), but these peaks are related to the Cu-Kβ and W-Lα signals, respectively. The W signal derives from the instrument, and it has nothing to do with the examined CuCrZr samples.

In the powder pattern, other small peaks are visible, while in the as-built samples they are absent. In particular, there are peaks at 45.1° and 65.7° (Figs. 16b and 16c). They could be related to the presence of intermetallic phases: for example, the Cu_5Zr manifests signals at those angles [33,34]. W signal is highly improbable since the element does not generate peaks in those positions [35,36].

Another small peak at 48° (visible in Fig. 16b) is instead common for the powder and the as-built samples, and this could be attributed to the presence of another intermetallic phase: $CuCrO_2$, for instance, generates signals at 35–38°, 48°, 62° and 66° [37,38]. The same peaks are also typical of many other Cu-based compounds, such as CuO [39] or $Cu_{51}Zr_{14}$ [27].

However, the peaks potentially related to Cu-Cr or Cu-Zr phases are very small and most of them are visible only on the powder, in the printed samples the signal is absent (also the DAHed samples were examined, but their diffractogram did not show differences compared to the as-built ones). This missing might be due to the reorganization of Cr,

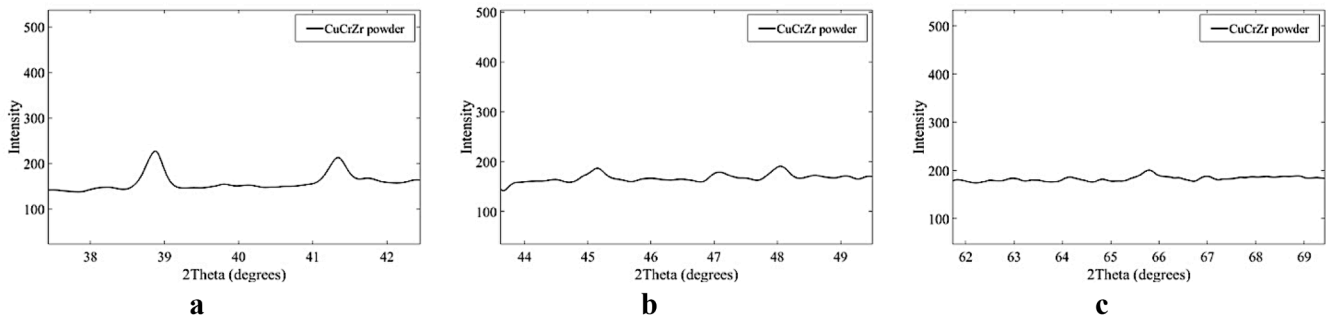

Fig. 16. a) Cu-kβ and W-kα show peaks at 39° and 41°, respectively; b) closeup on 45.1° and 48° peaks in powder signal; c) 65.7° peak in powder analysis.

Zr and O inside the Cu matrix: as it was seen at SEM, the precipitates could be too poor in number to generate a strong signal.

It is interesting to note that in the powder and vertical specimens the planes (111) and (020) are dominant, while in the horizontal sample, the greatest peak is the (022) one. The difference between the peaks intensity for as-built vertical and horizontal samples is due to the crystallographic orientation that is created during the printing process. A small shift in the position of the peaks in the vertical sample compared to the powder was also observed, the shift occurs also in the horizontal sample but is less visible. The change of the peaks position toward bigger angles might be due to the microstructural changes in terms of lattice dimensions that occur during printing.

Concerning the texture evaluation, a horizontal surface (the surface is parallel to the building platform) and a vertical surface (parallel to the building direction) of as-built samples were examined. The horizontal plane revealed a preferential orientation of the crystallites, while the vertical surface did not show preferential directions and the signal is equal for all the polar angles between 0 and 2π. The maps are reported in Fig. 17.

3.5. Micro-hardness

Hardness values did not show big discrepancies between the horizontal and vertical surfaces for all the examined samples.

The Vickers micro-hardness measurements are reported in Fig. 18. It is easy to understand that the hardness in the as-built conditions is low compared to the DAHed pieces: 1 h at 550 °C improved significantly this property (165 HV, which is twice the value for the as-built sample – 84 HV). Already after 3 h of treatment, samples started decreasing their maximum hardness (with a mean value of 144 HV), and after 6 h-long treatment, a further softening of the material occurred but also in this case there was an improvement with respect to the as-built state. This

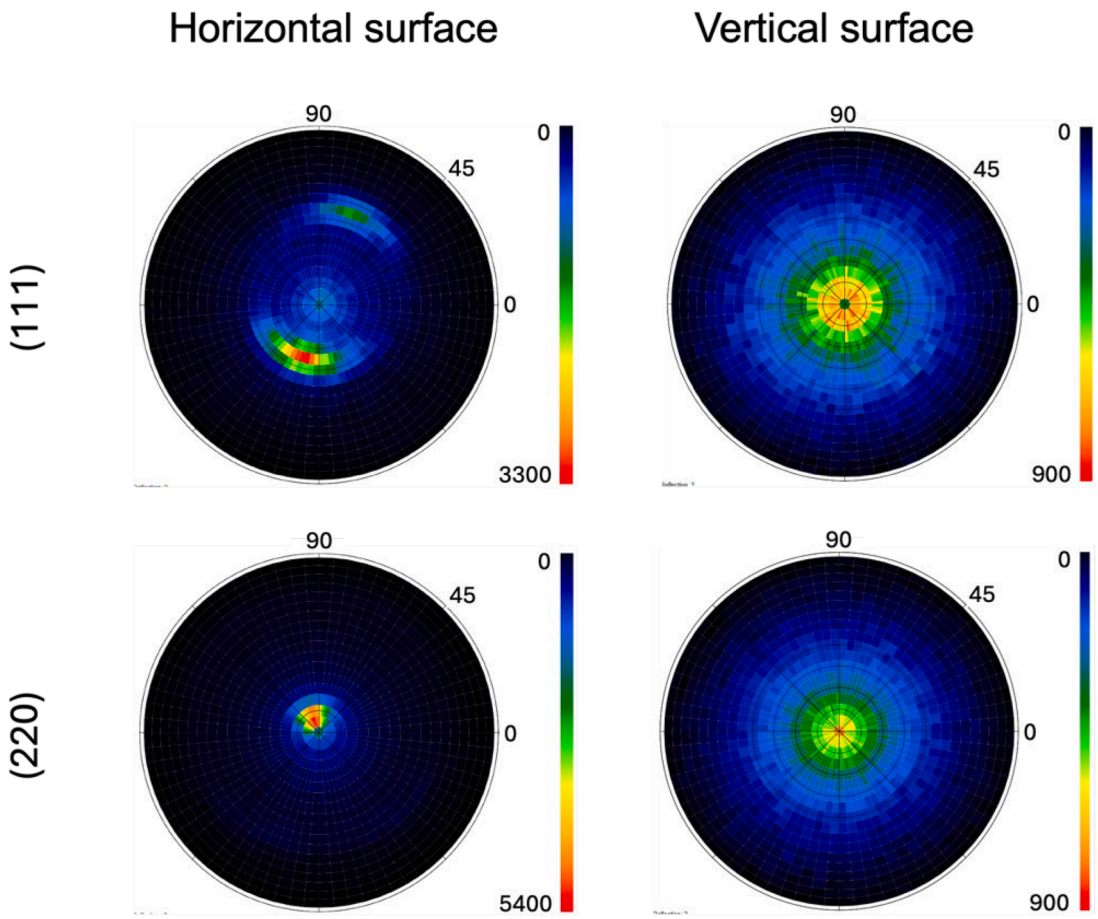

Fig. 17. Texture evaluation for horizontal and vertical samples (as-built).

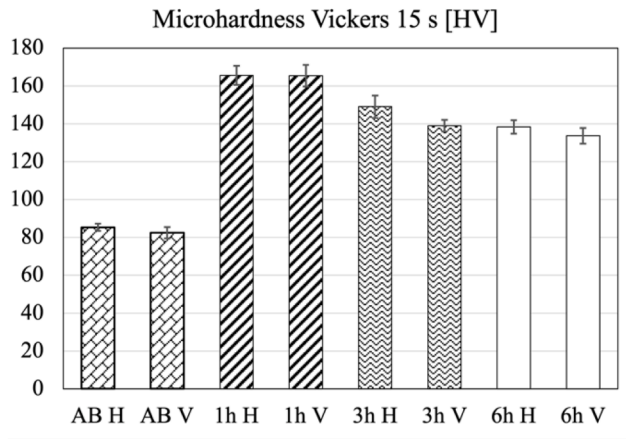

Fig. 18. Vickers microhardness values for the as-built and heat-treated samples.

means that a duration of 6 h is too long, leading to a coarsening of precipitates (overaging), as deduced also by the DSC analyses. The measures agree with the mechanical properties obtained from the tensile tests, as will be seen in the next section.

It is possible to see that 1 h is already effective in terms of improvement of the material hardness compared to the as-built condition.

3.6. Tensile tests

In Fig. 19, the stress-strain curves for all the samples are reported.

The dashed lines in Fig. 19 represent the vertical samples, while the solid lines correspond to the horizontal ones. There is a certain discrepancy between the two building directions for all the investigated conditions (as-built and heat-treated material). For example, considering the as-built samples (Fig. 19a), horizontal specimens show a higher mechanical strength since they reached higher stress values (UTS up to 258 MPa, while the vertical samples achieved 212 MPa), while the vertical samples showed a wider plastic region (total elongation of 34 %, against 31 % of horizontal pieces).

Average values of UTS, YS, total elongation El.% and elastic modulus E are reported in Table 2. As visible from Fig. 19, values in Table 2 confirm that the performed heat treatments are effective in increasing the material strength, while they reduce its ductility.

Concerning the 550 °C 1 h-long DAH (Fig. 19b, Table 2), the material increased considerably its strength: UTS and YS are almost twice the as-built values (up to 462 MPa and 377 MPa for the horizontal specimens, respectively) and are the maximum registered among the DAHs, while the total elongation is approximately 50% less than the not-treated material (12.8 % for the vertical test pieces). For this DAH, only two

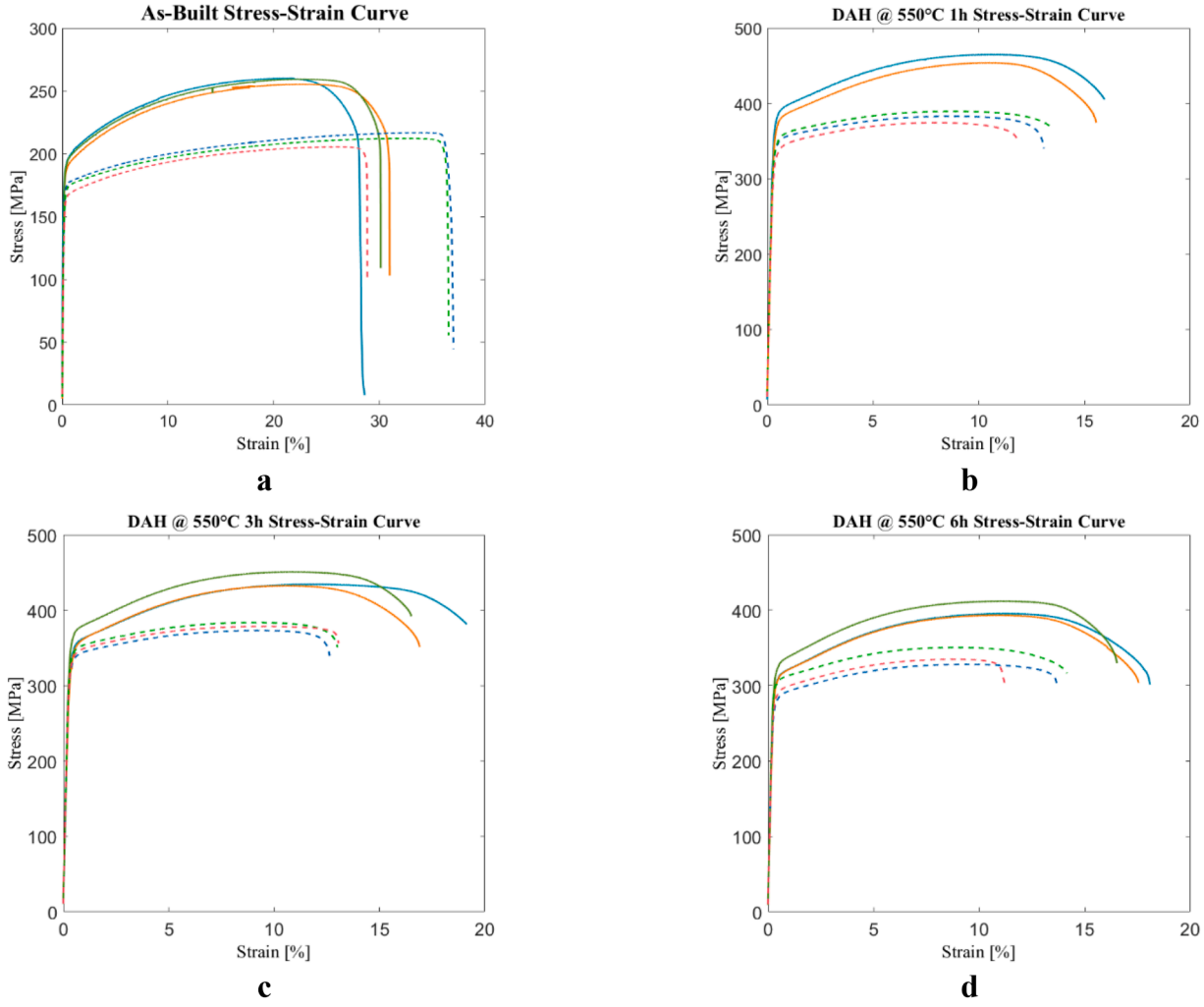

Fig. 19. Stress-Strain Curves for the CuCrZr in as-built state (a), after 1 h at 550 °C DAH (b), after 3 h at 550 °C DAH (c), and after 6 h at 550 °C DAH (d). The dashed lines indicate the stress-strain curves of vertical samples, while the horizontal samples are represented with solid lines.

Table 2
Tensile properties of investigated samples in terms of Ultimate Tensile Strength (UTS), Yield Strength (YS), Total Elongation (El.%) and Young's modulus (E).

	UTS [MPa]	YS [MPa]	El. [%]	E [GPa]
As-built Horizontal	258.36±2.5	189.61±3	31.8 ± 2.3	104.44±6.3
As-Built Vertical	212±6	155±5	34.1 ± 4.6	85.6 ± 2.1
550 °C 1 h Horizontal	462±11	377±7	15.8 ± 0.3	127.41±10.9
550 °C 1 h Vertical	382±8	341±8	12.8 ± 0.8	119.9 ± 3.2
550 °C 3 h Horizontal	439±10	353±12	17.5 ± 4.4	117.33±8.4
550 °C 3 h Vertical	379±5	336±6	12.9 ± 0.2	121.3 ± 0.1
550 °C 6 h Horizontal	400±10	313±8	17.4 ± 0.8	115±10.5
550 °C 6 h Vertical	338±11	291±11	13.0 ± 1.6	117.02±6.9

horizontal specimens were successfully tested since the third failed. The results are consistent with the Vickers micro-hardness results. With DAHs the elastic modulus increased, as well, but its value did not change significantly compared to the as-built condition: the Young's modulus E is almost constant after all the heat treatments without significant difference between horizontal and vertical directions. Generally, E was higher than 100 GPa, with the exception of the as-built vertical samples, which registered a modulus of 85.6 GPa.

1h-long and 3h-long treatments (Fig. 19b and 19c, respectively, and Table 2) were rather equivalent in terms of mechanical performance. Said so, 1h-long DAH is preferable because of the maximum mechanical performance achieved and the short duration of the treatment.

After 6 h (Fig. 19d, Table 2), there was a general decrease in the mechanical resistance, which means that an over-aging of the material took place: UTS and YS are lower compared to those recorded after the other DAHs. The total elongation instead did not show significant changes and was almost constant (in the range of 13 to 17 %).

Regarding the differences between the printing orientations, samples built along the vertical direction (i.e. parallel to the building direction) were always weaker than those built horizontally. This is due to the additive manufacturing process: in vertical samples, the gauge length is characterized by layer-layer interfaces that are perpendicular to the tensile force. Such interfaces are weak regions where fracture and cracks propagation are promoted [40]. Moreover, the load applied in tensile tests is also perpendicular to the LoFs that might be present inside the material: the poor interlayer bonding consequently affects the mechanical strength of the material in this direction since the fracture is favored at lower loads.

3.7. Thermal conductivity

The thermal conductivity of CuCrZr after each heat treatment was measured, according to the setup described in paragraph 2.8. The results are reported in Table 3.

The DAHed samples showed an increased value of thermal conductivity by more than three times compared to the as-built samples results. This is due to the precipitation phenomena: in an ideal scenario, once the Cr-Zr precipitates are formed from the saturated material, the Cu matrix no longer contains atoms that alter the crystalline structure of Cu, this increases the chemical purity and, thus, the thermal conductivity of the material, bringing it closer to that of pure copper.

The maximum thermal conductivity measured was 320 W/mK, and it was reached by the vertical sample heat-treated at 550 °C for 3 h.

Table 3
Thermal conductivity of CuCrZr in as-manufactured and heat-treated conditions, assessed both for vertical and horizontal printing directions.

Thermal Conductivity [W/mK]				
Printing direction	**As-Built**	**550 °C 1h**	**550 °C 3h**	**550 °C 6h**
Vertical	101±5	313±5	320±5	313±5
Horizontal	101±5	316±5	309±5	319±5

4. Discussion

The performed heat treatments determined a significant improvement in mechanical properties, such as hardness and tensile strength, especially after 1 h-long treatment.

This is due to the precipitation of strengthening particles containing Cu, Cr and Zr, as documented by DSC measurements. The precipitation started already during the printing process, as shown by SEM observations carried out in this work and TEM analyses that can be found in literature for the as-built CuCrZr [24–26]. Based on the DSC analyses, 1 h-long treatment at 500 °C is enough to complete the precipitation.

In fact, after the 3 h treatment, a decrease in hardness and strength was measured due to the overaging that occurs if the heat treatment duration exceeds the optimal time. During overaging, the precipitates agglomerate: such a structure is not optimal, because the bigger the particles, the lower their strengthening effect.

At the same time, the dislocations density decreases, because the higher the energy available (provided by keeping the material at high temperatures), the higher the number of dislocations that are able to overcome the obstacles. Therefore, they are free to move and annihilate.

As already mentioned, what was observed examining the mechanical properties is in good agreement with the DSC analyses: indeed, the absence of further precipitation mechanism after 1 h-long DAH is highlighted by the lack of peaks. This means that for longer durations of the heat treatments, only precipitates coarsening occurs. This can explain also the plateau observed in thermal conductivity measurements: if Cr and Zr dissolved again in the Cu matrix, the conductivity would decrease after longer DAHs; instead, the stability of this property suggests that the precipitation is not reversible and the overaging involves only a coarsening effect.

The hardness values measured in this work agree with what was found in other studies: Sun et al. [32] found an as-built hardness that ranges from 80 to 90 HV in case of energy density similar to the processed material described in this work. In addition, Salvan et al. [1] found hardness values of approximately 101 HV for the as-built sample, and Tang et al. [2] found 157 HV after 550 °C, 1 h-long DAH, which is similar to what was found in this study. It must be said that in those cases the load and the application time during the hardness assessment were different compared to the methodology considered in this paper. In addition, the CuCrZr powders and the manufacturing processes were different. However, the similarity with those results can show a certain repeatability and homogeneity of the as-built characteristics of this alloy.

In the literature, results are slightly different for some of the conditions examined in this work. In the present study, 550 °C 1 h DAH produced higher mechanical properties compared to what was obtained by Tang et al. [2] (UTS of 420±20 MPa and YS of 335±15 MPa), while their as-built CuCrZr showed completely different mechanical behavior compared to the as-built material described in this paper (UTS of 447 ±13 MPa, YS of 400±11 MPa and El.% of 10±3 %). Also, Salvan et al. [1] obtained a higher mechanical resistance from the as-built samples (UTS of 305±5 MPa, YS of 270±6 MPa and El.% of 26±2 %), while Wallis et al. [27] obtained mechanical properties that were closer to our results, regarding the as-built conditions (UTS of 287±2 MPa, YS of 204 ±1 MPa and El% of 33.2 ± 3.6 %).

Making a comparison with the already existing literature is difficult because of the huge variety of treatments already performed on the LPBFed CuCrZr. In most cases, the Age Hardening (AH) was carried out after a solution annealing (SA) treatment.

Concerning the thermal conductivity, the results are comparable with data already present in the literature, for CuCrZr processed with similar conditions: Tang et al. [2] tested CuCrZr with the same heat treatments, but they obtained a 6 % higher thermal conductivity in as-built and heat-treated material. This deviation is explained due to the different additive manufacturing processes. Indeed, Tang et al. CuCrZr printed with a 450 W green laser LPBF process, while in this work an

infrared 370 W laser was employed. In addition to this, they computed the thermal conductivities starting from electrical conductivity measurements, thus the Weidemann-Franz law was employed (thanks to which thermal conductivity can be calculated starting from the electrical conductivity results) considering the Lorenz constant obtained by Jadhav et al. [41]. The plateau of the thermal conductivity has been observed also by Wallis and Buchmayr [27], especially when DAHs above 500 °C are considered. They analyzed the CuCrZr alloy with similar LPBF process parameters. In this study, the thermal conductivity in as-built conditions was almost the same, but for DAHed material, Wallis and Buchmayr obtained lower results than the ones reported in this work. The differences are due to the different thermal conductivity measuring approaches: they employed the laser flash method [42] while the comparative-longitudinal heat flow was considered in this work.

Several studies in the existing literature reported no evidence of coarse Cr and Zr precipitates as the ones reported in Fig. 12 and 13 [1, 26,27]. Typically, in the as-built LPBFed CuCrZr is possible to see only a homogeneous single-phase-like structure [27]. However, different samples were investigated and micrometric scale areas rich in Cr and Zr were found also in the as-built parts, and not only in the heat-treated ones. Further investigations need to be carried out in order to understand how those areas are created during the printing process, if they can affect negatively the mechanical properties of the additively manufactured material, especially the fatigue resistance, and, if so, how the development of those structures can be avoided.

5. . Conclusions

This study investigated the performance achievable with the LPBF technology applied to the CuCrZr alloy. In particular, a low laser power (370 W) was employed to melt the powder and heat treatments (DAHs) were performed on the printed parts.

The fine cellular substructure inside the grains was still visible after heat-treating the material.

Nano-sized round particles were observed at very high magnification and they could be nanosized precipitates.

The mechanical properties enhanced considerably after 1 h-long DAH. Both the hardness and the tensile tests showed twice the values of the as-built samples (UTS of 253 MPa, YS of 172 MPa increased up to 422 MPa and 359 MPa, respectively, considering the averaged values between horizontal and vertical directions). Longer DAHs did not produce significant improvements, the 1 h-long DAH gave the highest Vickers micro-hardness (165 HV with 15 s dwell time).

The thermal conductivity improved after the DAHs, as well (300 W/mK). The different durations of the DAHs seemed not to significantly affect the thermal conductivity, and generally, horizontal specimens showed higher conductivity than vertical ones.

From the mechanical point of view, DAH treatments are promising for nuclear fusion applications, but investigation and treatment optimization need to be carried out to improve further the thermal conductivity, which remains too low.

CRediT authorship contribution statement

Valentina Candela: Writing – original draft, Visualization, Validation, Resources, Investigation, Conceptualization. **Luca Zanini:** Writing – review & editing, Investigation. **Marialaura Tocci:** Writing – review & editing, Supervision, Resources, Investigation, Conceptualization. **Massimiliano Bonesso:** Writing – review & editing, Conceptualization. **Carlo Scian:** Investigation. **Mourad El Idrissi:** . **Giacomo Favero:** Writing – review & editing, Investigation. **Michele Ballan:** Investigation. **Stefano Corradetti:** Investigation. **Razvan Dima:** Resources. **Girogio Keppel:** Resources. **Simone Mancin:** Resources. **Adriano Pepato:** Supervision, Resources. **Piergiorgio Sonato:** Supervision.

Declaration of competing interest

The authors declare that they have no known competing financial interests or personal relationships that could have appeared to influence the work reported in this paper.

Data availability

Data will be made available on request.

Fundings

This work has been carried out within the framework of the EUROfusion Consortium, funded by the European Union via the Euratom Research and Training Programme (Grant Agreement No 101052200 — EUROfusion). Views and opinions expressed are however those of the author(s) only and do not necessarily reflect those of the European Union or the European Commission. Neither the European Union nor the European Commission can be held responsible for them.

This work was developed with the financial support of Fondazione Cassa di Risparmio di Padova e Rovigo (CariPaRo).

References

[1] C. Salvan, L. Briottet, T. Baffie, L. Guetaz, C. Flament, CuCrZr alloy produced by laser powder bed fusion : microstructure, nanoscale strengthening mechanisms, electrical and mechanical properties, Mater. Sci. Eng. A 826 (2021) 141915, https://doi.org/10.1016/j.msea.2021.141915.

[2] X. Tang, X. Chen, F. Sun, L. Li, P. Liu, H. Zhou, S. Fu, A. Li, A study on the mechanical and electrical properties of high-strength CuCrZr alloy fabricated using laser powder bed fusion Xiangpeng, J. Alloys Compd. 924 (2022) 166627, https://doi.org/10.1016/j.jallcom.2022.166627.

[3] A.H. Seltzman, S.J. Wukitch, Nuclear response of additive manufactured GRCop-84 copper for use in Lower hybrid launchers in a fusion environment, Fusion Eng. Des. 159 (2020) 111726, https://doi.org/10.1016/j.fusengdes.2020.111726.

[4] T.I. El-Wardany, Y. She, V.N. Jagdale, J.K. Garofano, J.J. Liou, W.R. Schmidt, Challenges in three-dimensional printing of high-conductivity copper, J. Electron. Packag. Trans. ASME 140 (2) (2018) 1–12, https://doi.org/10.1115/1.4039974.

[5] V. Lindström, O. Liashenko, K. Zweiacker, S. Derevianko, V. Morozovych, Y. Lyashenko, C. Leinenbach, Laser powder bed fusion of metal coated copper powders, Materials 13 (16) (2020), https://doi.org/10.3390/MA13163493.

[6] S.D. Jadhav, P.P. Dhekne, S. Dadbakhsh, J.P. Kruth, J. Van Humbeeck, K. Vanmeensel, Surface modified copper alloy powder for reliable laser-based additive manufacturing, Addit. Manuf. 35 (2020) 101418, https://doi.org/10.1016/j.addma.2020.101418.

[7] S.D. Jadhav, P.P. Dhekne, E. Brodu, B. Van Hooreweder, S. Dadbakhsh, J.P. Kruth, J. Van Humbeeck, K. Vanmeensel, Laser powder bed fusion additive manufacturing of highly conductive parts made of optically absorptive carburized CuCr1 powder, Mater. Des. 198 (2021) 109369, https://doi.org/10.1016/j.matdes.2020.109369.

[8] G.M. Kalinin, A.D. Ivanov, A.N. Obushev, B.S. Rodchenkov, M.E. Rodin, Y. S. Strebkov, Ageing effect on the properties of CuCrZr alloy used for the ITER HHF components, J. Nucl. Mater. 367-370 B (2007) 920–924, https://doi.org/10.1016/j.jnucmat.2007.03.256. SPEC. ISS.

[9] R. Donnini, S. Kacilius, A. Mezzi, R. Montanari, N. Ucciardello, R. Volterri, "W thick coatings on CuCrZr for applications in future nuclear fusion reactors", La metallurgia Italiana, 103 (2011) 37–43, link: https://www.researchgate.net/publication/234556626_W_thick_coatings_on_CuCrZr_for_applications_in_future_nuclear_fusion_reactors.

[10] M. Lipa, A. Durocher, R. Tivey, Th. Huber, B. Schedler, J. Weigert, The use of copper alloy CuCrZr as a structural material for actively cooled plasma facing and in vessel components, Fusion Eng. Des. 75 (2005) 469–473, https://doi.org/10.1016/j.fusengdes.2005.06.056.

[11] A. Gusarov, C. Pohl, T. Pfalz, R. Bosch, S. Van Dyck, V. Barabash, R. Eaton, F. Zacchia, H. Samuli, Assessment of creep in reactor-irradiated CuCrZr alloy intended for the ITER T first wall panels, Fusion Eng. Des. 137 (2018) 112–123, https://doi.org/10.1016/j.fusengdes.2018.09.001.

[12] P. Agostinetti, E. Benedetti, T. Bolzonella, M. Bonesso, I. Casiraghi, R. Dima, G. Favero, A. Ferro, M. Gobbin, G. Granucci, C. Hu, P. Mantica, F. Lucchini, A. Pepato, N. Pilan, F. Raffaelli, P. Rebesan, A. Romano, G. Spizzo, F. Veronese, P. Vincenzo, Xie Yahong, Xie Yuanlai, Conceptual design of the beamline for the DTT neutral beam injector following a double beam source design approach, Plasma Fusion Res. 16 (2021), https://doi.org/10.1585/pfr.16.2405080.

[13] A. Pepato, G. Favero, M. Bonesso, M. Romanato, P. Rebesan, R. Dima, V. Candela, S. Candela, F. Veronese, P. Agostinetti, Implementation of the additive manufacturing for metals approach: the production of the acceleration grids for DTT NBI project, JACoW IPAC2023 (2023), https://doi.org/10.18429/JACoW-IPAC2023-TUPM018.

[14] P. Agostinetti, D. Aprile, V. Antoni, M. Cavenago, G. Chitarin, H.P.L. de Esch, A. De Lorenzi, N. Fonnesu, G. Gambetta, R.S. Hemsworth, M. Kashiwagi, N. Marconato, D. Marcuzzi, N. Pilan, E. Sartori, G. Serianni, M. Singh, P. Sonato, E. Spada, V. Toigo, P. Veltri, P. Zaccaria, Detailed design optimization of the MITICA negative ion accelerator in view of the ITER NBI, Nucl. Fusion 56 (2016), https://doi.org/10.1088/0029-5515/56/1/016015.

[15] P. Agostinetti, T. Bolzonella, M. Gobbin, P. Sonato, G. Spizzo, M. Vallar, P. Vincenzi, Conceptual design of a neutral beam heating & current drive system for DTT, Fusion Eng. Des. 146 (2019) 441–446, https://doi.org/10.1016/j.fusengdes.2018.12.087.

[16] D. Tiberto, U.E. Klotz, F. Held, G. Wolf, Additive manufacturing of copper alloys: influence of process parameters and alloying elements, Mater. Sci. Technol. 35 (8) (2019) 969–977, https://doi.org/10.1080/02670836.2019.1600840.

[17] M. Merola, A. Orsini, E. Visca, S. Libera, L.F. Moreschi, S. Storai, B. Panella, E. Campagnoli, G. Ruscica, C. Bosco, Influence of the manufacturing heat cycles on the CuCrZr properties, J. Nucl. Mater. 307–311 (2002) 677–680, https://doi.org/10.1016/S0022-3115(02)01186-8.

[18] C. Rotti, A.K. Chakraborty, I. Ahmed, G. Roopesh, M. Bandyopadhyay, M.J. Singh, Sejal Shah, A. Phukan, R.K. Yadav, N. Panda, K. Balasubramanian, Development of CuCrZr alloy for applications in neutral beams, in: Proceedings of the 2011 IEEE/NPSS 24th Symposium on Fusion Engineering, Chicago, IL, USA, 2011, pp. 1–5, https://doi.org/10.1109/SOFE.2011.6052213.

[19] S. Gorsse, C. Hutchinson, M. Gouné, R. Banerjee, Additive manufacturing of metals: a brief review of the characteristic microstructures and properties of steels, Ti-6Al-4V and high-entropy alloys, Sci. Technol. Adv. Mater. 18 (1) (2017) 584–610, https://doi.org/10.1080/14686996.2017.1361305.

[20] Z. Chen, P. Wei, H. Chen, X. Chen, Y. Ruan, W. Zhou, S. Lu, Laser powder bed fusion of k418 superalloy: process, microstructure, texture feature, and mechanical property, Metals 12 (4) (2022) 1–16, https://doi.org/10.3390/met12040611.

[21] S. Paul, J. Liu, S.T. Strayer, Y. Zhao, S. Sridar, M.A. Klecka, W. Xiong, A.C. To, A discrete dendrite dynamics model for epitaxial columnar grain growth in metal additive manufacturing with application to inconel, Addit. Manuf. 36 (2020) 101611, https://doi.org/10.1016/j.addma.2020.101611.

[22] M. Akbari, R. Kovacevic, Closed loop control of melt pool width in robotized laser powder–directed energy deposition process, Int. J. Adv. Manuf. Technol. 104 (2019), https://doi.org/10.1007/s00170-019-04195-y.

[23] Z. Li, Y. Chen, S. Zhang, B. Liu, Z. Kuai, W. Huo, H. Yang, M. Wei, P. Bai, Microstructure and properties in CuCrZr alloy fabricated by selective laser melting with different heat treatment, Results Phys. 54 (2023), https://doi.org/10.1016/j.rinp.2023.107125.

[24] L. Xu, Y. Zhang, L. Zhao, W. Ren, Y. Han, Performance improvement for the CuCrZr alloy produced by laser powder bed fusion using the remelting process, Materials (Basel) 17 (3) (2024), https://doi.org/10.3390/ma17030624.

[25] Z. Hu, Z. Du, Z. Yang, L. Yu, Z. Ma, Preparation of Cu-Cr-Zr alloy by selective laser melting: role of scanning parameters on densification, microstructure and mechanical properties, Mater. Sci. Eng. A 836 (2022), https://doi.org/10.1016/j.msea.2022.142740.

[26] K. Jahns, R. Bappert, P. Böhlke, U. Krupp, Additive manufacturing of CuCr1Zr by development of a gas atomization and laser powder bed fusion routine, Int. J. Adv. Manuf. Technol. 107 (5–6) (2020) 2151–2161, https://doi.org/10.1007/s00170-020-04941-7.

[27] C. Wallis, B. Buchmayr, Effect of heat treatments on microstructure and properties of CuCrZr produced by laser-powder bed fusion, Mater. Sci. Eng. A 744 (2019) 215–223, https://doi.org/10.1016/j.msea.2018.12.017.

[28] A. Vinogradov, V. Patlan, Y. Suzuki, K. Kitagawa, V.I. Kopylov, Structure and properties of ultra-fine grain Cu–Cr–Zr alloy produced by equal-channel angular pressing, Acta Mater 50 (2002) 1639–1651, https://doi.org/10.1016/S1359-6454(01)00437-2.

[29] K. Abib, F. Hadj Larbi, L. Rabahi, B. Alili, D. Bradai, DSC analysis of commercial Cu−Cr−Zr alloy processed by equal channel angular pressing, Trans. Nonferrous Met. Soc. China 25 (2015) 838–843, https://doi.org/10.1016/S1003-6326(15)63671-8.

[30] J. Zhou, Y. Huang, Z. Li, X. Tong, D. You, J. Yang, Q. Zhang, W. Li, X. Wang, Effect of heat treatments on microstructure mechanical and electrical properties of Cu-Cr-Zr alloy manufactured by laser powder bed fusion, Mater. Chem. Phys. 296 (2023), https://doi.org/10.1016/j.matchemphys.2022.127249.

[31] N. Ordás, L. Portolés, M. Azpeleta, A. Gómez, J.R. Blasco, M. Martinez, J. Ureña, I. Iturriza, Development of CuCrZr via Electron Beam Powder Bed Fusion (EB-PBF), J. Nucl. Mater. 548 (2021) 152841, https://doi.org/10.1016/j.jnucmat.2021.152841.

[32] F. Sun, P. Liu, X. Chen, H. Zhou, P. Guan, B. Zhu, Mechanical properties of high-strength cu–cr–zr alloy fabricated by selective laser melting, Materials 13 (21) (2020) 1–16, https://doi.org/10.3390/ma13215028.

[33] N. Köpfle, L. Mayr, D. Schmidmair, J. Bernardi, A. Knop-Gericke, M. Hävecker, B. Klötzer, S. Penner, A comparative discussion of the catalytic activity and CO2-selectivity of Cu-Zr and Pd-Zr (Intermetallic) compounds in methanol steam reforming, Catalysts 7 (2) (2017) 1–17, https://doi.org/10.3390/catal7020053.

[34] H. Shi, Y.-T. Zhou, R.-Q. Yao, W.-B. Wan, Q.-H. Zhang, L. Gu, Z. Wen, X.Y. Lang, Q. Jiang, Intermetallic Cu 5 Zr clusters anchored on hierarchical nanoporous copper as efficient catalysts for hydrogen evolution reaction, Research (2020), https://doi.org/10.34133/2020/2987234.

[35] L. Luo, J. Shi, J. Lin, X. Zan, X. Zhu, Q. Xu, Y. Wu, Microstructure and performance of rare earth element-strengthened plasma-facing tungsten material, Sci. Rep. 6 (2016), https://doi.org/10.1038/srep32701.

[36] K. Katayama, N. Ashikawa, F. Ding, H. Mao, H.S. Zhou, G.N. Luo, J. Wu, M. Noguchi, S. Fukada, Deuterium retention in deposited W layer exposed to EAST deuterium plasma, Nucl. Mater. Energy 12 (2017) 617–621, https://doi.org/10.1016/j.nme.2017.04.004.

[37] B. Yang, D. Ouyang, Z. Huang, X. Ren, H. Zhang, W.C.H. Choy, Multifunctional synthesis approach of In:cuCrO2 nanoparticles for hole transport layer in high-performance perovskite solar cells, Adv. Funct. Mater. 29 (34) (2019), https://doi.org/10.1002/adfm.201902600.

[38] D. Li, X. Fang, W. Dong, Z. Deng, R. Tao, S. Zhou, J. Wang, T. Wang, Y. Zhao, X. Zhu, Magnetic and electrical properties of p-type Mn-doped CuCrO2 semiconductors, J. Phys. D. Appl. Phys. 42 (5) (2009), https://doi.org/10.1088/0022-3727/42/5/055009.

[39] J.F. Xu, W. Ji, Z.X. Shen, S.H. Tang, X.R. Ye, D.Z. Jia, X.Q. Xin, Preparation and characterization of CuO nanocrystals, J. Solid State Chem. 147 (2) (1999) 516–519, https://doi.org/10.1006/jssc.1999.8409.

[40] M. Awd, F. Stern, A. Kampmann, D. Klemm, J. Tenkamp, F. Walther, Microstructural characterization of the anisotropy and cyclic deformation behavior of selective laser melted AlSi10Mg structures, Metals 8 (2018), https://doi.org/10.3390/met8100825.

[41] S.D. Jadhav, S. Dadbakhsh, R. Chen, R. Shabadi, J.-P. Kruth, J. Van Humbeeck, K. Vanmeensel, Modification of electrical and mechanical properties of selective laser-melted CuCr0.3 alloy using carbon nanoparticles, Adv. Eng. Mater. 22 (2019), https://doi.org/10.1002/adem.201900946.

[42] W.J. Parker, R.J. Jenkins, C.P. Butler, G.L. Abbott, Flash method of determining thermal diffusivity, J, Appl. Phys. 32 (9) (1961) 1679–1684, https://doi.org/10.1063/1.1728417.